View metadata, citation and similar papers at core.ac.uk
brought to you by CORE
provided by Repositorio Institucional de la Universidad de Alicante

PHYSICAL REVIEW A **69**, 062904 (2004)

# Coulomb-explosion imaging of $CH_2^+$: Target-polarization effects and bond-angle distribution

L. Lammich, H. Buhr, H. Kreckel, S. Krohn, M. Lange, D. Schwalm, R. Wester, and A. Wolf
*Max-Planck-Institut für Kernphysik, 69117 Heidelberg, Germany*

D. Strasser, D. Zajfman, and Z. Vager
*Weizmann Institute of Science, 76100 Rehovot, Israel*

I. Abril
*Departament de Física Aplicada, Universitat d'Alacant, Apartat 99, E-03080 Alacant, Spain*

S. Heredia-Avalos and R. Garcia-Molina
*Departamento de Física, Universidad de Murcia, Apartado 4021, E-30080 Murcia, Spain*

(Received 30 January 2004; published 15 June 2004)

The effect of target polarization fields on the bond-angle distribution following the foil-induced Coulomb explosion of $CH_2^+$ has been measured. Incorporating a detailed model description of the polarization effects and other target effects into a Monte Carlo simulation of the experiment, a good description of the various observables is obtained. In particular, the bond-angle distribution is found to agree with existing *ab initio* calculations.

DOI: 10.1103/PhysRevA.69.062904 PACS number(s): 34.50.Bw, 33.15.Dj

## I. INTRODUCTION

The technique of foil-induced Coulomb-explosion imaging (CEI) [1] has been used for analyzing the structure of simple molecular ions since many years. Yielding a direct picture of the nuclear geometry distribution, this technique provides information complementary to spectroscopic measurements of energy levels and transitions. The method is based on the fast stripping of binding electrons from molecular ions passing through a thin target foil at high velocities. The analysis of the relative velocities of the atomic fragments, which are influenced mainly by their mutual Coulomb repulsion, yields information on the initial nuclear geometry of the molecular ions, including vibrational excitations [2]. For a detailed understanding of the explosion process, a number of minor effects influencing the fragment trajectories have to be considered besides the dominant Coulomb repulsion. While most of these effects are well known and have been included in the standard data analysis procedure (such as multiple scattering and charge changing effects [3]), the dynamic polarization of the target material induced by the passage of the charged fragments (giving rise to the so called *wake fields* [4,5]) and its effect on the trajectories of neighboring fragments has never been fully integrated into the data reconstruction procedure; earlier measurements and simulations of dynamic polarization effects were performed only for diatomic molecular systems impinging on relatively thick targets [5–7].

The importance of the wake effect strongly depends on the types of atoms involved and the particular degrees of freedom to be investigated. In earlier CEI experiments [8], it proved to be sufficient to suppress polarization effects by restricting the analysis to molecules arriving at the target foil with a suitable orientation. However, such an "orientation cut" has the disadvantage of strongly reducing the statistics available (or to increase the measurement time) and is not applicable for more complex nonplanar molecular ions. Another approach is the empirical correction method applied in Ref. [9], which is also limited to simple molecules. In this work, we describe the inclusion of an *ab initio* description [10] of polarization effects in the data analysis procedure and its application in the CEI of $CH_2^+$. This specific molecular ion was chosen for three reasons: First, it includes a carbon atom which reaches relatively high charge states in the target foil and thus induces a pronounced wake field which can strongly modify the trajectories of the two lighter hydrogen atoms. Second, the $CH_2^+$ ion, as a fundamental carbon hydride ion, has raised interest in fields ranging from quantum chemical structure calculations to astrophysical applications [11,12], and has been a challenge to both experimental and theoretical approaches. Experimentally, $CH_2^+$ is a highly reactive ion and only recently a spectroscopic characterization of the vibrational ground state could be carried out [13], while the main challenge in the theoretical description and spectrum analysis is the presence of the Renner effect in the H-C-H bond angle [11]; in fact, it was a CEI experiment which was to show that $CH_2^+$ is bent [14]. And thirdly, in an earlier CEI experiment on $CH_2^+$ (Ref. [15]) performed in our laboratory, a small but conspicuous disagreement was found between the experimentally determined bond-angle distribution and theoretical calculations [16]. Several efforts have been made to search for the origin of this disagreement including extended calculations [17] to investigate the precision of the theoretical approach. Here, we report on a high-statistics CEI experiment and its analysis, which includes an improved treatment of the various target effects. Preliminary results from this investigation were already presented in a recent publication by Jensen *et al.* [11]; it is the goal of this paper to present the details of this analysis and to discuss the role of dynamic polarization effects on the bond angle distribution measurement of $CH_2^+$.

 ©2004 The American Physical Society

## II. EXPERIMENTAL ARRANGEMENT AND DATA ANALYSIS

### A. Technique and setup

The experiments presented here were carried out at the Coulomb-explosion imaging setup located at the Test Storage Ring (TSR) of the Max-Planck-Institut für Kernphysik in Heidelberg, Germany [18]. A beam of 6.7 MeV $CH_2^+$ ions was formed by fragmentation of a 4.7 MeV $CH_3O^-$ ion beam, which was produced by a sputter ion source, in the stripper gas at the terminal of a tandem Van de Graaf accelerator. The ions were then injected into the storage ring and kept circulating for up to 15 s. The residual background gas pressure in the ring was of the order of $\sim 5 \times 10^{-11}$ mbar. During this time, a small fraction of the beam was continuously extracted from the TSR and guided toward the CEI setup. This method allows the stored molecular ions to cool their rovibrational excitations via radiative transitions, and to follow this relaxation by time-dependent measurements. For $CH_2^+$, excited vibrational levels in the stretching and bending modes have lifetimes below 30 and 300 ms, respectively [19]; hence, after $>2$ s of storage the nuclear conformation distributions of the molecular ions can be examined in equilibrium with the 300 K background radiation, i.e., basically in the vibrational ground state [15].

The molecular ions extracted from the storage ring were directed toward targets with thicknesses in the range of $\sim 50-100$ Å; in the present experiment, "diamondlike-carbon" (DLC) foils [20] were used. When the fast molecular ions hit the foil, the binding electrons as well as most valence electrons are stripped off the nuclei in a very short time ($\sim 0.1$ fs). The remaining atomic ions repel each other through their mutual Coulomb interaction, and the asymptotic momenta of the Coulomb explosion fragments are reached after $\sim 10$ fs, corresponding to a flight distance of $\sim 1000$ Å. These asymptotic momenta and the final ion charge states of the fragments are analyzed for each single molecule with the help of two three-dimensional imaging detectors located $\sim 3$ m downstream from the target. In the experiment on $CH_2^+$ described here, carbon ions were produced in charge states ranging from 2 to 5 together with two protons. At a distance of $\sim 0.4$ m from the target, the fragment ions were slightly steered by a magnetic field which directed the protons and the carbon ions toward two separate imaging detectors. On the carbon imaging detector, ions with different charge states were clearly separated. The asymptotic fragment velocities in the center-of-mass frame after Coulomb explosion can thus be derived from the impact positions and times on the imaging detectors for each charge state separately. More details about the experimental setup can be found in Ref. [18].

### B. Coulomb-explosion imaging simulations and target effects

According to the estimates given above, the largest part of the Coulomb explosion takes place behind the foil with the fragments in ionic charge states which can be deduced from their deflection in the magnetic field. Hence, the Coulomb explosion technique can largely take advantage of the simplicity of the force law describing the repulsion between the fragment ions. However, for a detailed analysis of CEI data, a number of more subtle effects must be considered regarding the interaction of the molecular fragments with the atoms and electrons of the target foil as well as in the subsequent evolution of the fragment momenta behind the foil.

Specifically, the following effects while traversing the target foil are expected: (a) The charge state of the fragment can vary by electron capture and stripping processes, (b) the momenta of the fragments may be modified by close collisions with (screened) atomic nuclei in the foil, (c) the Coulomb interaction between the fragments may be modified through a static screening of the fragment charges, and (d) dynamic polarization effects of the foil medium may induce additional forces on the fragment ions. Only the first three effects have been taken into account so far in the analysis of Coulomb explosion data using a Monte Carlo simulation, which follows the time development of the molecular dissociation process through the target [3]; issue (d), which concerns not only the wake forces but also energy loss processes, has so far not been included. The simulation starts from a given initial molecular structure and a random overall orientation of the incident molecule relative to the foil, and takes into account additional experimental parameters like the profile of the ion beam, the resolution of the detectors and the geometry of the setup. The code finally produces a sample of simulated events which can be compared directly to experimental data. Through this comparison, the experimental data yields information on the validity of the theoretical model underlying the geometrical molecular structure used as input for the simulation.

Beside the effects caused by the target material, the electronic structure of the molecular fragments may in some cases affect the dissociation process especially after the target foil. By collisions occuring during the passage through the foil, electrons still bound to the fragments may end up in excited states. These electrons are usually much less localized in configuration space than the ground-state electrons, and as a consequence, other fragments of the same molecule may, at the short internuclear distances still present directly after the target foil, be repelled by a potential which is stronger than the potential caused by a well localized charge distribution. The incomplete screening of the nuclear charge by excited electrons thus leads to the observation of increased asymptotic velocities. This effect can be included in the simulation by using molecular orbitals to describe the dissociating, highly charged system. However, this would imply the need for a theoretical model of these orbitals as well as for the population of different electronic states of the system, thus compromising the advantage of the CEI method of being largely independent of theoretical predictions.

To minimize the influence of extended charge state contributions of the fragments on the results of CEI experiments, only events with emerging fragments in high charge states should be used in the data analysis. In the specific case of $CH_2^+$, the main interest lies in the bond-angle distribution of the molecule, which is expected to be hardly affected by such screening effects: In this quasilinear molecule, the Coulomb repulsion works mainly between the carbon fragments and the protons, while the mutual repulsion of the two protons is relatively weak. Thus the bond angle is barely

changed by the actual Coulomb-explosion process and can be analyzed without the need of detailed knowledge of the radial gradient of the carbon-proton potential.

An additional important input parameter for the CEI simulations is the thickness of the target foil used in the experiment. To measure this value for the DLC foils used in the present work, an additional experiment was performed using atomic ions as projectiles. The broadening of these atomic beams due to nuclear collisions in the target foil [see effect (b) above] was then compared to simulation results, and the effective target thickness was determined as the value yielding the best agreement between simulation and experiment. The effective target thickness deduced using this procedure was found to be independent of the types of ions and beam energies, suggesting that the description of the scattering processes used in the simulation [3] is correct and that the effective thickness determined in this way can be considered to be a good measure of the geometrical thickness of the target foil; the accuracy of the extracted target thickness is estimated to be of the order of ~10%.

### C. Geometrical considerations specific to $CH_2^+$

As pointed out above, the asymptotic velocities of the three fragments relative to each other contain the information on the internal structure of the incoming molecules, and their orientation in space is correlated to the orientation of the molecule when hitting the target foil. As is customary, the coordinates describing the spatial position of the nuclei in the center-of-mass frame of the *incoming* molecule will be referred to as *R*-space coordinates, while the relative asymptotic fragment velocities will be called *V*-space coordinates. The following geometrical definitions hold both in *R* space and in *V* space, although it is important to recall that only the *V*-space coordinates are measured directly.

The internal geometry of the molecules is described in *R* space by the lengths $r_i$ $(i=1,2)$ of the two C-H bonds and by the bond angle $\alpha_R$. For the fragmentation pattern in *V* space, the corresponding relative velocities $V_i$ between the two H fragments and the C fragment, as well as the opening angle $\alpha$ between the relative velocity vectors $\boldsymbol{V}_i$ are chosen.

The orientation of any nonlinear triatomic molecular structure in space can be described by two angles defining the orientation of the plane spanned by the three nuclei, plus one angle defining the orientation of the molecule within this molecular plane. Taking the beam direction as the reference direction $\boldsymbol{z}$, the orientation of the molecular plane is denoted by the angle $\Theta_R$ between its normal vector $\boldsymbol{n}$ and the $\boldsymbol{z}$ axis (see Fig. 1). The orientation of the projection of $\boldsymbol{n}$ onto the $(x,y)$ plane, which is perpendicular to the beam and coincides with the target plane, is denoted by $\Phi_R$. Due to the symmetry of the arrangement, no dependences on the angle $\Phi_R$ are expected in the present case. To characterize the orientation of the triatomic structure in the molecular plane, we define a $\boldsymbol{z}'$ axis in the molecular plane by its intersection with the plane spanned by $\boldsymbol{z}$ and $\boldsymbol{n}$, and a vector $\boldsymbol{m}$ by the bisecting line of the H-C-H angle, as indicated in Fig. 1. We then describe the orientation of the molecule within the molecular plane by the angle $\Psi_R$ between $\boldsymbol{z}'$ and $\boldsymbol{m}$. The cosine of the orientation angle $\Theta_R$ of the molecular plane varies between $\cos\Theta_R=1$ (the molecule is oriented parallel to the target foil) and $\cos\Theta_R=0$ (the molecule is oriented perpendicular to the target foil). The angle $\Psi_R$ varies between 0 and $\pi$ and (for $\cos\Theta_R>0$) describes whether the two hydrogen atoms travel in front of the carbon atom ($\Psi_R=0$) or behind it ($\Psi_R=\pi$).

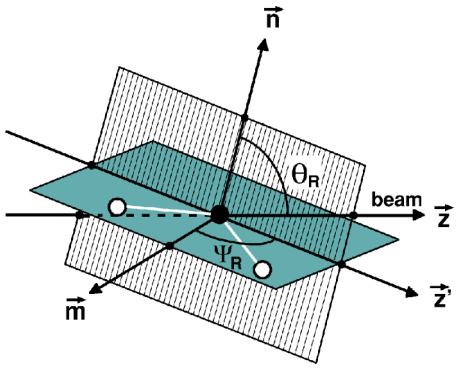


FIG. 1. Definition of the orientation angles $\Theta_R$ and $\Psi_R$ of the $CH_2^+$ molecule, the carbon (hydrogen) ion being depicted by the black (open) circle. The vectors $\boldsymbol{n}$ and $\boldsymbol{m}$ describe the normal vector on the molecular plane and the bisecting line of the H-C-H bond angle, respectively.

Referring to the *V* space, the quantities cos Θ, Φ, and Ψ will be used below to discuss the dependences of the relative fragment velocity distributions and event rates on the observed orientation of the fragmenting molecule. The quantities cos $\Theta_R$, $\Phi_R$, and $\Psi_R$, referring to the *R* space and used as input parameters for the Monte Carlo simulation, are all uniformly distributed for an ensemble of incident molecules with random orientation.

## III. EXPERIMENTAL RESULTS

Using the procedure described in Sec. II A, a total number of $\sim 8\times10^5$ $CH_2^+$ fragmentation events were recorded over a total storage time of 15 s. The dominant carbon charge states produced behind the target foil were $q=3$ and 4 with fractions amounting to 0.3 and 0.6, respectively. Since the electrons in the heliumlike ion $C^{4+}$ are less likely to be excited to levels where they may only partially screen the nuclear charge than the outer electron of the lithiumlike charge state $C^{3+}$, the analysis was restricted to events with $q=4$ carbon ions in coincidence with two protons as discussed in Sec. II B.

In order to monitor the vibrational relaxation of the $CH_2^+$ ions, the fragmentation geometry characterized by the relative velocities $V_i$ and the H-C-H opening angle $\alpha$ was analyzed as a function of the storage time. Following an initial narrowing of the $V_i$ and $\alpha$ distributions, no further time dependence was found after 2 s of storage, indicating complete relaxation of the internal degrees of freedom (thermal equilibrium at 300 K, corresponding to >99% in the vibrational ground state). The measurements were performed with two different DLC targets of $0.8\pm0.1$ and $1.5\pm0.2$ $\mu g/cm^2$, respectively, determined as described in Sec. II B. In the fol-

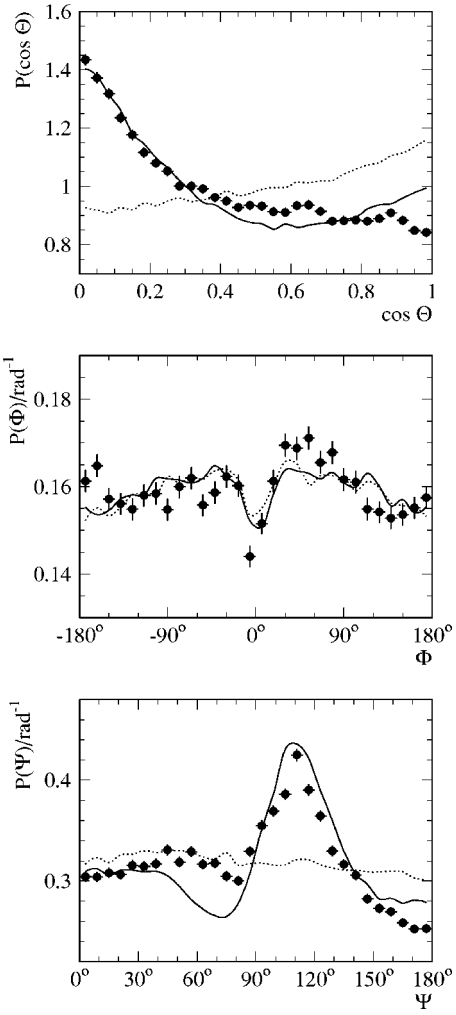


FIG. 2. Probability distributions for the observing events at different orientation angles Θ, Φ, and Ψ. Experimental data (circles) obtained with a 1.5 $\mu g/cm^2$ target are compared to simulations including (solid lines) and neglecting (dotted lines) dynamic polarization effects.

lowing, data recorded after 2 s of storage using the 1.5 $\mu g/cm^2$ target are shown as polarization effects are more clearly seen when using a thicker target foil.

Figure 2 displays the probabilities $P(\cos\Theta)$, $P(\Phi)$, and $P(\Psi)$ for observing a molecule with an orientation angle Θ, Φ, and Ψ. Assuming that the initial molecules are randomly oriented in $R$ space before entering the foil, these $V$-space distributions should be uniform in the absence of any target effects and detector biases. The measured distributions, however, are clearly nonuniform and show strong disturbancies which have to be attributed to polarization effects: The molecular plane in $V$ space is found to be most likely oriented perpendicular to the target foil ($\cos\Theta=0$), and the distribution of the angle Ψ has a pronounced maximum at $\sim 110°$.

The measured normalized bond angle distribution $P(\cos\alpha)$, integrated over all measured orientations, is shown in Fig. 3. The distribution peaks at $\cos\alpha \approx -0.77$. To examine the influence of the polarization fields on the measured bond-angle distribution, we characterise this distribution by two parameters, $(\cos\alpha)_{max}$ and $P_{max}$, which describe the position and the height of the maximum of the probability distribution, respectively. The value of $(\cos\alpha)_{max}$ is a measure of the most probable bond angle, while $P_{max}$ is correlated to the "sharpness" of the distribution.

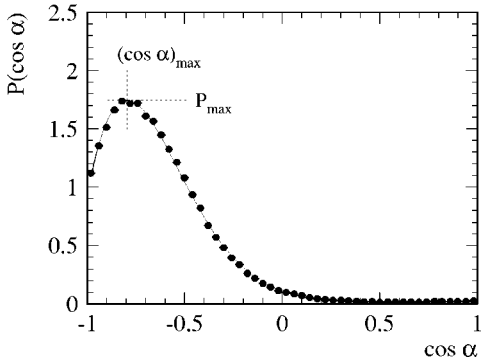


FIG. 3. Measured distribution of the H-C-H angle $\alpha$. The normalized histogram data are fitted by a smooth function. The position $(\cos\alpha)_{max}$ and height $P_{max}$ of its maximum will be used to investigate the influence of dynamic polarization effects on this distribution.

Figures 4 and 5 show the measured dependence of $(\cos\alpha)_{max}$ and $P_{max}$, respectively, on the orientation Θ, Φ, or Ψ of the molecule in $V$ space; the two characteristic quantities are plotted against each of the three external angles whose probability distributions where shown in Fig. 2. The data presented in Figs. 4 and 5 show that both $(\cos\alpha)_{max}$ and $P_{max}$ depend only slightly on the orientation angles Θ and Φ of the molecular plane, while both quantities show a strong dependence on the angle Ψ, which describes the orientation of the molecule within this plane. Large extrema are observed for both $(\cos\alpha)_{max}$ and $P_{max}$ around $\Psi=90°$, showing that also the measured bond angle distribution is affected by the polarization fields (see Sec. V).

## IV. TREATMENT OF TARGET POLARIZATION EFFECTS

### A. Dielectric formalism

The motion of a charged particle through a solid disturbs the electronic density of the latter in such a manner that an induced electric field appears. This field extends approximately in a conical shape behind the projectile, with an oscillatory intensity that decays exponentially with distance [4,21]. The induced electric field results in a stopping force which slows the particle down, the negative value of that force being the so-called stopping power (or energy loss per unit path length). When a fast molecule passes through a solid, it dissociates in the first atomic layers, resulting into an ensemble of charges moving in close proximity. The electric field induced by each one of these charges, besides slowing them down, also modifies the velocities of neighboring fragments, giving rise to the so-called wake forces.

At nonrelativistic particle velocities the total force $\boldsymbol{F}_i$ exerted by an ensemble of moving charges $q_j$ and their induced electric fields onto a selected particle $i$ of this ensemble is given at any instant by

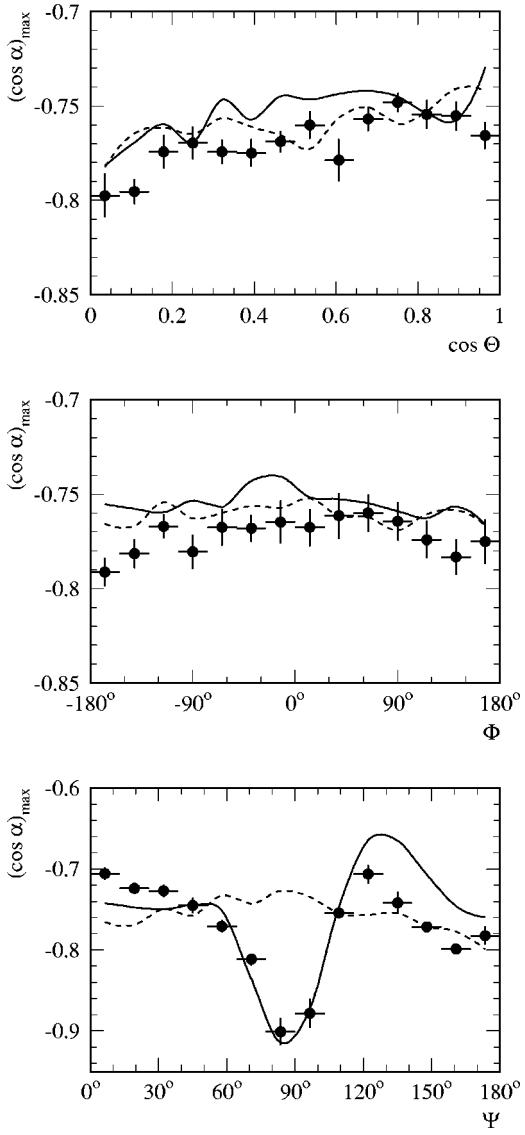


FIG. 4. The most probable bond angle $(\cos\alpha)_{\max}$ of the normalized bond-angle distribution for different orientation angles $\Theta$, $\Phi$, and $\Psi$. Experimental data (circles) obtained with a 1.5 $\mu$g/cm$^2$ target are compared to simulations including (solid lines) and neglecting (dotted lines) dynamic polarization effects.

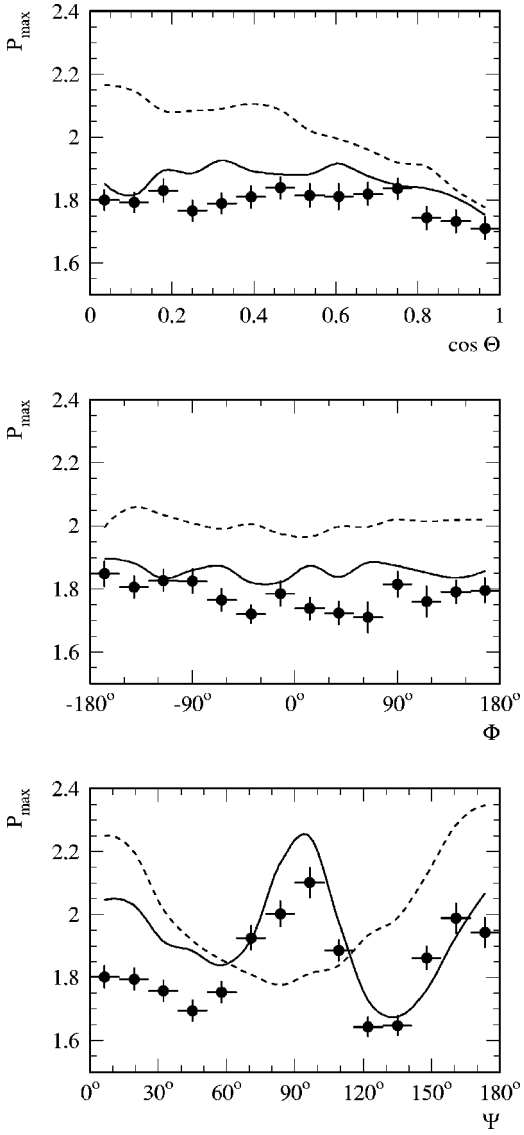


FIG. 5. Height $P_{\max}$ of the normalized bond angle distribution at different orientation angles $\Theta$, $\Phi$, and $\Psi$. Experimental data (circles) obtained with a 1.5 $\mu$g/cm$^2$ target are compared to simulations including (solid lines) and neglecting (dotted lines) dynamic polarization effects.

$$\boldsymbol{F}_i = \sum_{j\neq i} \boldsymbol{F}_{i,j}^{\mathrm{coul}} + \sum_j \boldsymbol{F}_{i,j}^{\mathrm{pol}}. \tag{1}$$

Here $\boldsymbol{F}_{i,j}^{\mathrm{coul}}$ is the usual Coulomb force acting between particle $j$ and $i$, while $\boldsymbol{F}_{i,j}^{\mathrm{pol}}$ denotes the force on $i$ caused by the polarization of the medium by particle $j$, the latter term containing both the stopping force (for $i=j$) and the wake force (for $i\neq j$). Note, that by writing down Eq. (1), we have assumed that the polarization fields can be added linearly. As the electric field induced by a moving charge in an isotropic medium has cylindrical symmetry around its motion axis, it is convenient to use cylindrical coordinates $r_\parallel$ and $r_\perp$ to describe the position $\boldsymbol{r}_{i,j}$ of the particle $i$ relative to the instantaneous position and velocity direction $\boldsymbol{v}_j/v_j$ of the particle $j$. Using the dielectric formalism [22–24], the cylindrical components of the polarization force $\boldsymbol{F}_{i,j}^{\mathrm{pol}}$ are found to be (in atomic units)

$$F_{i,j\parallel}^{\mathrm{pol}}(r_\parallel, r_\perp) = \frac{2}{\pi v_j^2}\int_0^\infty \mathrm{d}k \frac{\rho_i(k)\rho_j(k)}{k}\int_0^{kv_j} \mathrm{d}\omega\ \omega \times J_0\left(r_\perp\sqrt{k^2-\frac{\omega^2}{v_j^2}}\right)\left\{\sin\left(\frac{\omega r_\parallel}{v_j}\right)\times \mathrm{Re}\left[\frac{1}{\epsilon(k,\omega)}-1\right] + \cos\left(\frac{\omega r_\parallel}{v_j}\right)\mathrm{Im}\left[\frac{1}{\epsilon(k,\omega)}\right]\right\}, \tag{2}$$

and

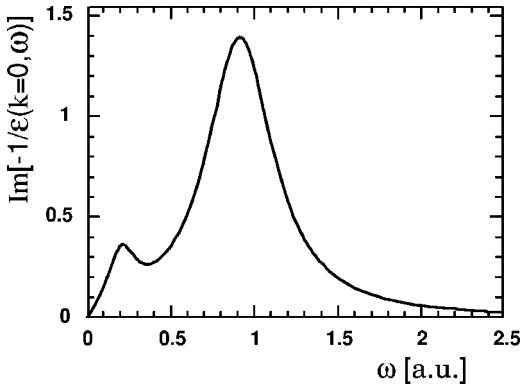


FIG. 6. Energy loss function of amorphous carbon, obtained from a fit of optical data (see Ref. [32]) as discussed in Refs. [26,27].

$$F_{i,j\perp}^{\mathrm{pol}}(r_{\parallel},r_{\perp}) = \frac{2}{\pi v_j}\int_0^{\infty} \mathrm{d}k \frac{\rho_i(k)\rho_j(k)}{k} \int_0^{kv_j} \mathrm{d}\omega \sqrt{k^2-\frac{\omega^2}{v_j^2}} \times J_1\left(r_{\perp}\sqrt{k^2-\frac{\omega^2}{v_j^2}}\right)\left\{\cos\left(\frac{\omega r_{\parallel}}{v_j}\right) \times \mathrm{Re}\left[\frac{1}{\epsilon(k,\omega)}-1\right]-\sin\left(\frac{\omega r_{\parallel}}{v_j}\right)\mathrm{Im}\left[\frac{1}{\epsilon(k,\omega)}\right]\right\}. \tag{3}$$

Here $\epsilon(k,\omega)$ is the dielectric function describing the response of the medium to an external perturbation in terms of the momentum and energy transfer $k$ and $\omega$, respectively, $\rho(k)$ denotes the Fourier transform of the charge distribution of a moving particle (reducing to $q$ for a point charge), and $J_0(\ldots)$ and $J_1(\ldots)$ are Bessel functions of the first kind [25].

For $i=j$, i.e., $\boldsymbol{r}_{i,j}=0$, $F_{\perp}$ is vanishing and $F_{\parallel}$ reduces to the stopping force $F_i^{\mathrm{stop}}$, which is given by

$$F_i^{\mathrm{stop}} = F_{i,i\parallel}^{\mathrm{pol}} = -\frac{2}{\pi v_i^2}\int_0^{\infty} \mathrm{d}k \frac{\rho_i(k)^2}{k} \int_0^{kv_i} \mathrm{d}\omega\ \omega\ \mathrm{Im}\left[\frac{-1}{\epsilon(k,\omega)}\right]. \tag{4}$$

Moreover, by replacing $\mathrm{d}\omega\ \omega$ by $\mathrm{d}\omega\ \omega^2$, Eq. (4) leads to the energy loss straggling, which characterizes the fluctuation in the energy loss per unit path length.

The energy loss function, $\mathrm{Im}[-1/\epsilon(k,\omega)]$, plays a key role in the dielectric formalism. We have presented elsewhere [26,27] a procedure to determine the energy loss functions (and $\mathrm{Re}[1/\epsilon(k,\omega)]$) of target materials in a realistic manner from measured optical excitation spectra. The deduced energy loss functions reproduce satisfactorily the main characteristics (peak positions, widths and intensities) of the electronic excitation spectra, they fulfil the $f$-sum rule [28], and they result in a reasonable prediction of the mean excitation energy $I$ [29] of the material. For the DLC targets employed in the present experiment, we have used the energy loss function derived in Ref. [26] for amorphous carbon (see Fig. 6) as the energy loss function is not known for the ultrathin DLC foils used in the present experiment. These foils are optimized for minimal thickness and uniformity rather than hardness and chemical inertness, and their mass density of $2.0\pm0.2$ g/cm$^3$ [20] is closer to that of arc evaporated amorphous carbon foils than to the density of (thicker) DLC films which have an optimal fraction of diamondlike $sp^3$ bonds [30]. However, as the measured energy loss functions of these DLC films are still rather close to that of amorphous carbon, our approximation seems to be reasonable; it will get its final justification by the quality of the description of the polarization effects reached in our analysis.

At the velocity relevant in this work ($v_i=4.4$ a.u.), each $CH_2^+$ molecular ion dissociates inside the foil into two protons and one carbon ion, whose charge state varies dynamically as a result of electronic capture and loss processes. For the description of wake forces, it was found sufficient in the present case to treat all fragments as point charges, while in the calculation of the stopping power the electronic structure of the atomic ions had to be taken into account; the required Fourier transform of the charge density corresponding to an ion with atomic number $Z$ and $N$ bound electrons was taken from the Brandt–Kitagawa model [31] and reads

$$\rho(k) = Z - \frac{N}{1+(k\Lambda)^2}, \tag{5}$$

where

$$\Lambda = \frac{0.48N^{2/3}}{Z-N/7}. \tag{6}$$

### B. Inclusion of wake effects in the Coulomb-explosion imaging simulation

To include the effects of dynamic target polarization into the existing CEI simulation code [3], two additional forces have to be taken explicitly into account in the equations of motion for each fragment $i$, the stopping force $\boldsymbol{F}_i^{\mathrm{stop}}$ and the wake force $\Sigma_{j\neq i}\boldsymbol{F}_{i,j}^{\mathrm{pol}}$.

The stopping force corresponding to the momentary charge state of the fragment is looked up in a table, which contains the stopping force and its fluctuation for all possible charge states of the atoms involved in the experiment. This table is precalculated according to Eq. (4) for the beam velocity in use. The direction of this force is set antiparallel to the momentary direction of motion of the fragment.

The wake effect is taken into account by adding up the forces acting on a fragment due to the wake fields induced by all other fragments. Each of the binary forces $\boldsymbol{F}_{i,j}^{\mathrm{pol}}$ is calculated by projecting the position of the "probe" fragment $i$ into the cylindrical coordinate frame defined by the instantaneous velocity of the "source" fragment $j$. The wake forces in this frame are then looked up in another precalculated table representing the results of Eqs. (2) and (3). Finally, these forces are transformed back to the standard Cartesian coordinates and are used, together with the stopping and interparticle Coulomb forces, as input to the integration algorithm of the equations of motion; as the static screening approach considered in the existing CEI code by modifying the

Coulomb forces [issue (c) in Sec. II B] is replaced by a dynamic polarization treatment, unscreened interparticle Coulomb forces are now being used.

As a statistical process, the straggling of the energy loss depends nonlinearly on the distance travelled by the fragment. Thus, it can not be represented by a force and included in the integration of the equations of motion. Instead, at the end of a path segment, obtained by integrating the equations of motion between two successive nuclear scattering events (see Ref. [3]), the calculated energy loss is modified by adding (subtracting) an additional energy loss, which is taken from a Gaussian distribution using a variance calculated as discussed in Sec. IV B.

We would like to point out, that the present treatment of the dynamic polarization effects neglects surface effects due to the finite thickness $D$ of the target material, which is of the order of $D=50-100$ Å in our experiments. However, the typical extension $d$ of the wake fields is given by (in a.u.) $\omega \cdot d/v_i = \pi$, which results in $d \approx 7$ Å for the most likely $\omega$ of $\omega \approx 1$ a.u. (see Fig. 6). Thus, we find for the different length scales $r_{ij} < d < D$, suggesting that the approximation is reasonable.

## V. EXPERIMENT AND TARGET POLARIZATION EFFECTS

Because of their anisotropy, polarization effects are likely to introduce orientation dependences as observed in Sec. III. Using the simulation algorithm described above, these dependences can now be analyzed in detail and compared to the experimental data. To make the comparison easier, an additional simulation neglecting all effects of target polarization except for the static screening of the Coulomb potential was performed. The first simulation will be referred to as *dynamic simulation* and its results are shown as solid lines in Figs. 2, 4, and 5, while the second one (dashed lines) is referred to as *static simulation*. The molecular geometry input of the simulation is based on the work of Osmann *et al.* [17], with an equilibrium bond angle of $\alpha_R = 140.5°$ and an internuclear C-H distance of $r_i = 1.096$ Å.

### A. Orientation distributions

Figure 2 shows the effect of the polarization force on the measured orientation of the molecule. The preference for small values of $\cos\Theta$ observed in the experimental $P(\cos\Theta)$ distribution is well reflected by the dynamic simulation while it is absent in the static one. This aligning effect, which is due to the polarization forces dragging the protons into the wake of the carbon fragment, has been observed and discussed already in early experiments by Gemmell *et al.* [7]. In contrast $P(\Phi)$, which reflects the distribution of the projection of the molecular plane normal $\boldsymbol{n}$ onto the plane perpendicular to the beam direction, is as expected almost flat and independent of wake effects because of symmetry reasons; the only relevant feature in the $P(\Phi)$ distribution is a dip at $\Phi \approx 0$, which corresponds to a reduced detection efficiency for vertically aligned protons, which is well understood and reproduced by both simulations.

The dynamic simulation of the probability distribution $P(\Psi)$ results in a pronounced peak at $\Psi \approx 110°$, in agreement with the experiment, but displays in addition a dip at $\Psi \approx 70°$, which is not born out by the data. The maximum can be understood if one takes into account that for an average bond angle of $\alpha_R \approx \alpha \approx 140°$, one of the protons will be aligned for $\Psi \approx 110°$ behind the leading carbon atom, an orientation that is expected to be preferred considering the negative polarization charge following the carbon fragment. At $\Psi \approx 70°$, on the other hand, one of the protons is travelling in front of the carbon atom, and the deviation between the calculation and the experimental data might indicate that the simulation is overestimating the force that de-aligns a leading proton. For the static simulation, as expected, no dependence of the number of events on $\Psi$ is visible.

As depicted in Fig. 2 for the thicker (1.5 $\mu g/cm^2$) of the two targets investigated, the overall agreement between the experiment and the dynamic simulation for the probability distributions $P(\cos\Theta)$, $P(\Phi)$, and $P(\Psi)$ is better than 10%, and the same level of accuracy has been reached in describing the distributions obtained with the thinner target of 0.8 $\mu g/cm^2$. The comparison shows, that our *ab initio* treatment of the wake effects results in a rather accurate description of the reorientation effects caused by the dynamic target polarization. The origin of the remaining differences may be due to imperfections in our present understanding of the polarization effect or due to the various approximations made in the derivation of the polarization forces and by their inclusion into the simulation program (see Sec. IV). In particular, we disregarded possible surface effects, which might modify the polarization fields in the proximity of the target foil surfaces or lead to additional effects even after the molecular fragments have left the target.

### B. Bond-angle distribution

After having discussed the influence of the polarization forces on the distribution of the events with respect to the three orientation angles $\cos\Theta$, $\Phi$, and $\Psi$ as well as the accuracy which has been reached in describing these distributions, we now turn to the discussion of the influence of the polarization forces onto the bond angle distribution.

As shown in Fig. 4, the most probable bond angle $(\cos\alpha)_{max}$ was found to have only a weak dependence on the orientation given by $\Theta$ and $\Phi$, in agreement with both the static and dynamic simulation. Both simulations predict the same smooth trend even though $P(\cos\Theta)$ is influenced by the wake field (see Fig. 2). In contrast, $(\cos\alpha)_{max}$ does show a strong dependence on the orientation angle $\Psi$ due to the dynamic target polarization effects, which can be traced at least qualitatively to the geometry of the molecule and the definition of $\Psi$ (see Fig. 1). At $\Psi = 0°$, both protons are travelling ahead of the carbon fragment, and the polarization charge induced in the target, which is mainly located behind the multiply charged carbon fragment, is expected to have only little influence on the bond angle. As $\Psi$ increases, one of the protons gets closer to the wake of the carbon fragment

and thus feels an attractive force which tends to further open the bond angle, that is, to decrease the value of $(\cos\alpha)_{\max}$. This behavior is clearly visible in the experimental data and well reproduced by the dynamic simulation, while the static simulation predicts $(\cos\alpha)_{\max}$ to be independent of $\Psi$. At larger values of $\Psi$, the force aligning the trailing proton with the carbon fragment reaches a maximum and then decreases, finally vanishing at an orientation already exhibiting a maximum alignment of the two fragments; as pointed out above this happens at $\Psi\approx 110°$ for a bond angle of $\approx 140°$. For even higher values of $\Psi$, the same force is reducing the bond angle, leading to increased values of $(\cos\alpha)_{\max}$ as seen in Fig. 4 at $\Psi\approx 120°$.

Even though the $\Psi$ dependence of $(\cos\alpha)_{\max}$ is influenced by polarization effects, when averaged over $\Psi$ the mean bond angle is rather independent of these effects as judged from the close similarity of the measured $\Theta$ and $\Phi$ dependence of $(\cos\alpha)_{\max}$ with both the static as well as the dynamic simulation. Averaging over all orientation angles the overall deviation of the simulated $(\cos\alpha)_{\max}$ from the experimental value corresponds to less than 1.5° in the mean bond angle.

Additional effects of the dynamic polarization of the target material are observed in the measured orientation dependence of the height $P_{\max}$ of the bond-angle distribution $P(\cos\alpha)$, which reflects the sharpness of the distribution. As shown in Fig. 5, the dependence of $P_{\max}$ on $\cos\Theta$ shows reasonable agreement between the experiment and the dynamic simulation, while the static simulation is overestimating the sharpness of the bond-angle distribution for small values of $\cos\Theta$, that is, for orientations where the molecular plane is not parallel to the target foil. This is due to the fact that the static simulation is lacking a mechanism which causes fluctuations of the velocities $\boldsymbol{v_i}$ of the individual fragments in the beam ($z$) direction. In the dynamic simulation, and obviously also in the experiment, such fluctuations are produced by the polarization forces, which exhibit a statistical nature due to the changing charge states of the ions inducing the fields, and due to statistical variations in the energy loss. These fluctuations will, in general, lead to a smearing of the measured probability distributions of the internal molecular coordinates, but depending on the direction of the velocity fluctuations and on the orientation of the molecule, the internal coordinates will be affected differently. For a triatomic molecule oriented parallel to the target foil ($\cos\Theta\approx 1$), a fluctuation of $v_z$ mainly changes the orientation of the molecule, while a scattering in the $x$ or $y$ direction operates within the molecular plane and thus changes the bond lengths or the bond angle. Therefore, at this orientation, only velocity fluctuations transversal to the beam direction will smear out the bond-angle distribution and thus reduce $P_{\max}$. Fluctuations in the $x,y$ plane, however, are mainly generated by multiple collisions of projectile fragments on the target nuclei, which are well described already in the static simulation code. Therefore, the agreement of experiment and both simulations is reasonably good at $\cos\Theta\approx 1$. For decreasing $\cos\Theta$ values, the molecular plane is more and more tilted with respect to the target foil and thus processes which cause a scattering in beam direction gain influence on the bond-angle distribution. In fact, at these orientations, the dynamic simulation is still able to reproduce the experimental data to within 5% in contrast to the static simulation, which is lacking a fluctuation process working in the beam direction.

Similar effects are also visible in the dependence of $P_{\max}$ on $\Psi$. For $\Psi\approx 0°$ and $\Psi\approx 180°$, again mainly the velocity fluctuations in $z$ direction will smear out the bond-angle distribution; thus the static prediction results in a too sharp bond-angle distribution. At intermediate $\Psi$, also the nuclear scattering in the $x$ and $y$ directions influence the measured bond angle, which decreases the value of $P_{\max}$ predicted by the static simulation. On the other hand, the dynamic simulation, as well as the experiment, results in a maximum of $P_{\max}$ at $\Psi\approx 90°$, which is due to an overcompensation of the statistical smearing processes by a systematic change of bond angles due to the polarization forces acting at this orientation; the force aligning a trailing proton with the carbon fragment not only leads to a systematic increase of the bond-angles (see Fig. 4), but also to a focusing of the bond-angle distribution.

The dependence of $P_{\max}$ on the orientation angle $\Phi$ is again smooth as expected from symmetry arguments. However, the presence of the fluctuations caused by the polarization effects in the dynamic simulation leads to a considerably better description of the measured value of $P_{\max}$. When averaged over all molecular orientations, the deviation of the simulated $P_{\max}$ from the experimental value decreases from about +13% for the static to less than +4% for the dynamic simulation.

## VI. DISCUSSION

The analysis of the orientation and bond-angle distributions have revealed a significant influence of dynamical polarization effects on the results deduced from a CEI experiment. In previous CEI experiments [8], we minimised this influence by including in the data analysis only certain orientations of the molecules believed to be least sensitive to polarization effects, a procedure which results in losses of statistics and cannot be used for nonplanar molecules. Since the orientation dependence is now largely reproduced by simulations which include the dynamic polarization of the target foil, we can now use the complete data set to study the structure of the molecule of interest and to investigate the consistency of the deduced molecular structure results regarding various target and other effects which have to be considered in a careful analysis of a CEI experiment.

For the $CH_2^+$ molecule investigated in the present work, the normalized bond-angle distributions $P(\rho_V)$ measured at the two target thicknesses of 0.8 $\mu g/cm^2$ and 1.5 $\mu g/cm^2$ are compared to the results of our dynamic simulation in Fig. 7. The angle $\rho_V = 180° - \alpha$ was used so that a more direct comparison with the theoretical work of Jensen *et al.* [11] can be performed; note, however, that the present $\rho_V$ is measured in $V$ space and has to be distinguished from the corresponding $\rho_R$ angle defined in $R$ space. Figures 7(a) and 7(c) show the results for the thin and thick target, respectively, requiring $\Theta$ to obey $\cos\Theta > 0.8$, while Figs. 7(b) and 7(d)

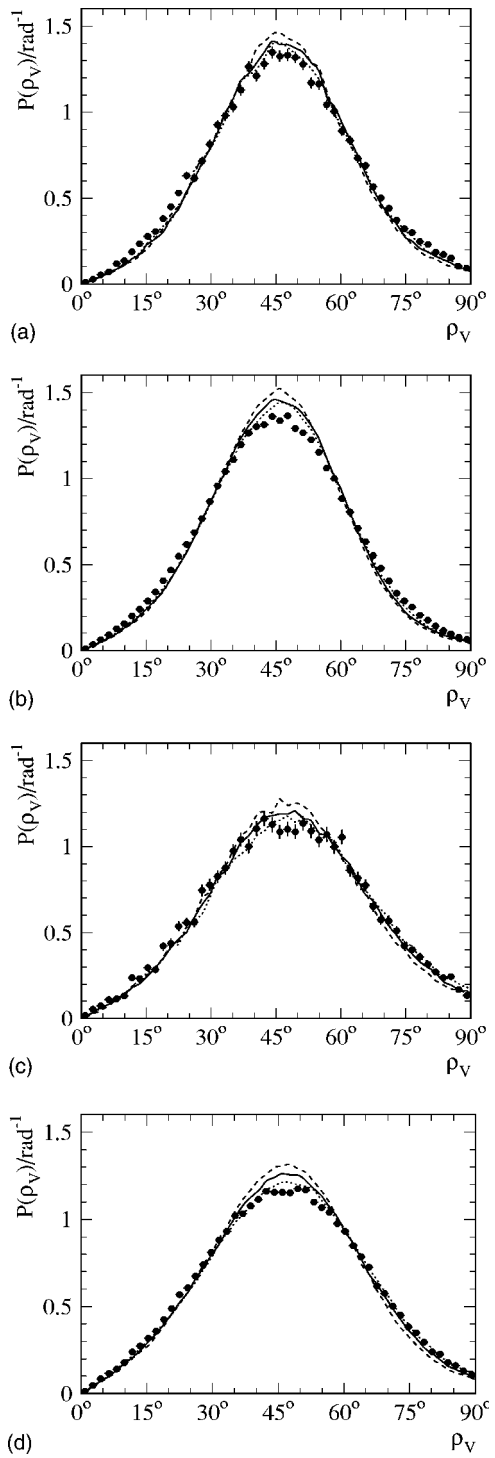


FIG. 7. Probability distribution of the bond angle supplement $\rho_V = 180^\circ - \alpha$. Experimental data (circles) are compared to simulations including dynamic polarization effects (solid lines). Dashed and dotted lines denote the uncertainty in the simulation by allowing the target thickness to vary within its error: (a) Thin target, for $\cos\Theta > 0.8$, (b) thin target, all orientations, (c) thick target, for $\cos\Theta > 0.8$, and (d) thick target, all orientations.

are obtained allowing all orientation angles to contribute [the results shown in Fig. 2 of Ref. [11] correspond to a slightly earlier stage of the data analysis and simulation of the distribution shown in Fig. 7(a)]. As expected, the probability distributions $P(\rho_V)$ are noticeably sharper for the thinner of the two targets [Figs. 7(a) and 7(b)] due to the reduction of scattering and polarization effects in the foil. Dashed and dotted lines represent the results of our dynamic simulations when varying the target thickness within its uncertainty.

The orientation cut employed in Figs. 7(a) and 7(c) is identical to the cut used in our previous work on $CH_2^+$ (Ref. [15]) to avoid a deterioration of the CEI results by the wake fields; in fact, our present investigations show (see Figs. 4 and 5), that the observed bond-angle distribution is indeed not sensitive to dynamic polarization effects for $\cos\Theta > 0.8$. Being able to now include these effects into our analysis, the $P(\rho_V)$ distributions with and without orientation cuts are now found to be equally well represented by our simulation. However, as observed already in our detailed analysis of $P_{\max}$ in the previous section, the measured distributions are still marginally broader than the simulated ones. For example, the $P(\rho_V)$ distributions shown in Fig. 7(d) for the thick target and no orientation cut correspond to mean $\rho_V$ values of 46.4(1)° for the experimental data and 46.5(3)° for the simulation results, while the full width at half maximum amounts to 45.0(1)° for the experiment and 42.8(1.3)° for the simulation. In the case of the simulation, the errors are dominated by the uncertainty of the target thickness. The slightly larger widths of the experimental $P(\rho_V)$ distributions point to additional small broadening contributions not yet considered in our simulations. Among them are surface effects which modify the polarization fields in the proximity of the target foil surfaces, and quantum effects which come mainly from the fact that the initial kinetic energy of the molecule in the ground vibrational state is not taken into account in the classical description of the Coulomb explosion used in our simulation program (see Ref. [2]). While these contributions will be masked in experiments with thicker targets by the fluctuations caused by small angle scattering and polarization effects already included in our simulations, they will gain importance in experiments performed with extremely thin targets. Indeed, the additional broadening needed to achieve perfect agreement between experiment and simulation seems to increase for decreasing target thickness. There might also be some imperfections in the potential energy surface used for calculating the wave function, however this cannot be addressed by the present level of accuracy reached in this CEI experiment.

Bearing in mind the various approximations made in the treatment of the target effects and the description of the Coulomb explosion process, the amount of agreement between experimental and simulated *V*-space data obtained suggests that the geometry of the $CH_2^+$ molecular ion is well described by the calculated *R*-space structure [17] used as input for the simulation algorithm. The agreement is certainly better than the one reached in Refs. 9 and 15, where the treatment of target effects was not complete. Since the comparison done in Ref. 15, the improvements achieved include a change of target material [20], a more advanced method to determine the target thickness (Sec. II B), the addition of polarization effects (Sec. IV) in the simulation algorithm, and several smaller improvements in the experimental setup and data analysis. Moreover, by comparing *V*-space rather

than *R*-space distributions, one avoids additional uncertainties introduced by the unfolding process.

The results achieved in the present work represent the outcome of combined efforts in the fields of molecular theory, solid-state theory, and CEI experiments in order to clarify the structure of the $CH_2^+$ ion. The broad and intense search for possible problems in all of these fields has finally lead not only to a good agreement of experiment and theory, but also to a better understanding of the effect of wake fields in foil induced CEI experiments.

**ACKNOWLEDGMENTS**

This work has been supported in part by the German-Israel Foundation for Scientific Research (GIF) under Contract No. I-707-55.7/2001, the Spanish Ministerio de Ciencia y Tecnología (Project Nos. BFM2003-04457-C02-01/02 and HA2001-0052), the DAAD in the framework of the Acciones Integrados Program 2002/03, and the European Community within the Research Training Network "Electron Transfer Reactions." One of the authors (S.H.A.) thanks the Fundación Cajamurcia for a Postdoctoral Grant.

[1] Z. Vager, R. Naaman, and E. P. Kanter, Science **244**, 426 (1989).
[2] Z. Amitay, A. Baer, M. Dahan *et al.*, Phys. Rev. A **60**, 3769 (1999).
[3] D. Zajfman, G. Both, E. P. Kanter, and Z. Vager, Phys. Rev. A **41**, 2482 (1990).
[4] N. Bohr, and K. Dan K. Dan. Vidensk. Selsk. Mat. Fys. Medd. **18**, No. 8 (1948).
[5] Z. Vager and D. S. Gemmell, Phys. Rev. Lett. **37**, 1352 (1976).
[6] A. Faibis, R. Kaim, I. Plesser, and Z. Vager, Nucl. Instrum. Methods **170**, 99 (1980).
[7] D. S. Gemmell, J. Remillieux, J.-C. Poizat, M. J. Gaillard, R. E. Holland, and Z. Vager, Nucl. Instrum. Methods **132**, 61 (1976).
[8] H. Kreckel, S. Krohn, L. Lammich *et al.*, Phys. Rev. A **66**, 052509 (2002).
[9] Z. Vager, Adv. At., Mol., Opt. Phys. **45**, 203 (2001).
[10] R. Garcia-Molina, C. D. Denton, I. Abril, and N. R. Arista, Phys. Rev. A **62**, 012901 (2000).
[11] P. Jensen, T. E. Odaka, W. P. Kraemer, T. Hirano, and P. R. Bunker, Spectrochim. Acta, Part A **58**, 763 (2002).
[12] V. G. Anicich and W. T. Huntress, Jr., Astrophys. J., Suppl. Ser. **62**, 553 (1986).
[13] S. Willitsch and F. Merkt, J. Chem. Phys. **118**, 2235 (2003).
[14] T. Graber, E. P. Kanter, Z. Vager, and D. Zajfman, J. Chem. Phys. **98**, 7725 (1993).
[15] A. Baer, M. Grieser, L. Knoll, J. Levin, R. Repnow, D. Schwalm, Z. Vager, R. Wester, A. Wolf, and D. Zajfman, Phys. Rev. A **59**, 1865 (1999).
[16] W. P. Kraemer, P. Jensen, and P. R. Bunker, Can. J. Phys. **72**, 871 (1994).
[17] G. Osmann, P. R. Bunker, W. P. Kraemer, and P. Jensen, Chem. Phys. Lett. **309**, 299 (1999).
[18] R. Wester, F. Albrecht, M. Grieser *et al.*, Nucl. Instrum. Methods Phys. Res. A **413**, 379 (1998).
[19] A. Baer, Ph.D. thesis, Weizmann Institute of Science, Rehovot, Israel, (2000).
[20] J. Levin, L. Knoll, M. Scheffel, D. Schwalm, R. Wester, A. Wolf, A. Baer, Z. Vager, D. Zajfman, and V. K. Liechtenstein, Nucl. Instrum. Methods Phys. Res. B **168**, 268 (2000).
[21] P. M. Echenique, F. Flores, and R. H. Ritchie, Solid State Phys. **43**, 229 (1990).
[22] E. Fermi, Phys. Rev. **57**, 485 (1940).
[23] R. H. Ritchie, Phys. Rev. **114**, 644 (1959).
[24] J. Lindhard and A. Winther, K. Dan. K. Dan. Vidensk. Selsk. Mat. Fys. Medd. **34**, No. 4 (1964).
[25] M. Abramowitz and I. A. Stegun, eds., *Handbook of Mathematical Functions* (Dover, New York, 1972).
[26] I. Abril, R. Garcia-Molina, C. D. Denton, F. J. Pérez-Pérez, and N. R. Arista, Phys. Rev. A **58**, 357 (1998).
[27] J. C. Moreno-Marín, I. Abril, and R. Garcia-Molina, Nucl. Instrum. Methods Phys. Res. B **193**, 30 (2002).
[28] D. Y. Smith, *Handbook of Optical Constants of Solids* (Academic Press, Orlando, 1985).
[29] ICRU Report 49, *Stopping Powers and Ranges for Protons and Alpha Particles* (International Comission on Radiation Units and Measurements, Bethesda, Md., 1993).
[30] S. Waidmann, M. Knupfer, J. Fink, B. Kleinsorge, and J. Robertson, J. Appl. Phys. **89**, 3783 (2001).
[31] W. Brandt and M. Kitagawa, Phys. Rev. B **25**, 5631 (1982).
[32] J. Cazaux and D. Gramari, J. Phys. (France) Lett. **38**, L133 (1977).